PHYSICAL REVIEW B **77**, 184413 (2008)

Melting of magnetic correlations in charge-orbital ordered $La_{1/2}Sr_{3/2}MnO_4$: Competition of ferromagnetic and antiferromagnetic states

D. Senff,[1] O. Schumann,[1] M. Benomar,[1] M. Kriener,[1,2] T. Lorenz,[1] Y. Sidis,[3] K. Habicht,[4] P. Link,[5,*] and M. Braden[1,†]
[1]*II. Physikalisches Institut, Universität zu Köln, Zülpicher Strasse 77, D-50937 Köln, Germany*
[2]*Department of Physics, Kyoto University, Kyoto 606-8502, Japan*
[3]*Laboratoire Léon Brillouin, CEA/CNRS, F-91191 Gif-sur-Yvette Cedex, France*
[4]*Hahn-Meitner-Institut, Glienicker Strasse 100, D-14109 Berlin, Germany*
[5]*Forschungsneutronenquelle Heinz Maier-Leibnitz (FRM II), TU München, Lichtenbergstrasse 1, D-85747 Garching, Germany*
(Received 11 January 2008; published 13 May 2008)

The magnetic correlations in the charge and orbital ordered manganite $La_{1/2}Sr_{3/2}MnO_4$ have been studied by elastic and inelastic neutron scattering techniques. Out of the well-defined charge exchange (CE)-type magnetic structure with the corresponding magnons, a competition between CE-type and ferromagnetic fluctuations develops. Whereas ferromagnetic correlations are fully suppressed by the static CE-type order at low temperature, elastic and inelastic CE-type correlations disappear with the melting of the charge-orbital order at high temperature. In its charge-orbital disordered phase, $La_{1/2}Sr_{3/2}MnO_4$ exhibits a dispersion of ferromagnetic correlations, which remarkably resembles the magnon dispersion in ferromagnetically ordered metallic perovskite manganites.

DOI: 10.1103/PhysRevB.77.184413 PACS number(s): 75.30.Ds, 71.10.−w, 75.47.Lx, 75.50.Ee

I. INTRODUCTION

Charge ordering is one of the key elements to understand colossal magnetoresistivity (CMR) in the manganite oxides. The large drop of the electric resistivity at the metal-insulator transition can only partially be explained by the Zener double-exchange mechanism.[1] The larger part of it seems to arise from the competition between ferromagnetic (FM) metallic and charge ordered insulating states, and recent experimental and theoretical investigations focus on electronically soft phases and phase separation scenarios.[2–6] The metal-insulator transition can be considered as the stabilization of the FM metallic phase over charge ordered insulating states by an external parameter as, e.g., temperature or magnetic field.[7,8]

At half doping, the insulating, charge-orbital ordered (COO) phase appears most stable, and an ordered state appears as a generic feature in the phase diagrams of cubic manganites $R_{1-x}A_xMnO_3$ (R=La or rare earth, A=Sr,Ba,Ca,…),[7] as well as in those of single- and double-layered systems, such as $La_{1/2}Sr_{3/2}MnO_4$ and $LaSr_2Mn_2O_7$.[9,10] In spite of its relevance for the CMR effect and in spite of the enormous number of publications in this field, the properties of the charge ordered state are not fully established up until now. Early investigations on $La_{0.5}Ca_{0.5}MnO_3$ by Wollan and Koehler[11] and by Goodenough[12] proposed a checkerboard ordering of charges with sublattices of Mn^{3+} and Mn^{4+} sites. Simultaneously, the single e_g orbitals on the Mn^{3+} sites order in a stripelike pattern, which give rise to zigzag paths with each e_g orbital bridging two Mn^{4+} neighbors with $3d^3$ configuration and an empty e_g level (see Fig. 1). This orbital arrangement implies a FM ordering along the zigzag chains and an antiferromagnetic (AFM) coupling between adjacent chains, which are referred to as CE-type ordering,[11] and it explains the observed structural and magnetic superlattice reflections in diffraction experiments.[13,14] More recently, an alternative model, consisting of a coherent ordering of magnetic dimers, called Zener polarons, has been proposed,[15] which is fundamentally different. Whereas in the initial model charge and orbital ordering is located on the Mn sites, the alternative model proposes the ordering of charges to be located on the Mn-O-Mn bonds. The two concepts remain a matter of strong controversy[16–21] with the more recent work favoring the initial site-centered model. In particular, for $La_{1/2}Sr_{3/2}MnO_4$, there is strong evidence that the bond-centered model cannot be applied.[20] One should, however, consider the possibility that different manganites exhibit different types of charge-orbital order. Furthermore, it is important to emphasize that the site-centered model of charge and orbital ordering is only schematic. Different crystallographic studies[10,18,22–25] find structural distortions in the charge ordered phase, which are far smaller than what is expected for

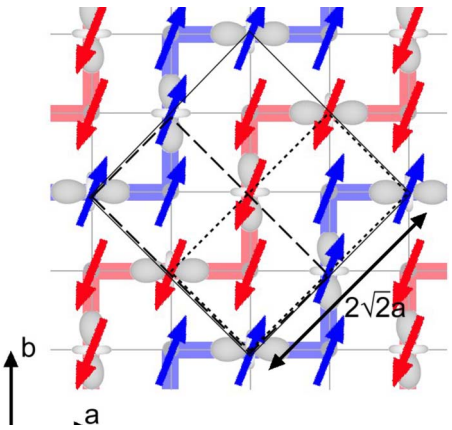

FIG. 1. (Color online) Schematic representation of the charge, orbital, and spin ordering in the CE-type arrangement, as proposed by Goodenough (Ref. 12). The orbital and the magnetic lattices of the Mn^{3+} subsystem are indicated by the dotted and dashed lines, respectively. Notice that the zigzag chains run along the [110] direction.

a full integer ordering into Mn^{3+} and Mn^{4+} valencies. Nevertheless, throughout this paper, we will use this Mn^{3+}/Mn^{4+} nomenclature for clarity.

The origin of the charge ordered state is also under debate, and different theoretical studies focus on very different aspects. It has been shown that the COO state can be primarily stabilized by cooperative Jahn–Teller distortions. In this scenario, the magnetic ordering of the CE type appears as a secondary effect.[26–28] On the other hand, it has been argued that based on anisotropic magnetic exchange interactions, the COO can be stabilized by purely electronic effects.[29,30] In this sense, the COO state is of magnetic origin, which naturally explains its melting in magnetic fields.[29,31,32]

The single-layered material $La_{1/2}Sr_{3/2}MnO_4$ is particularly well suited for the experimental investigation of the properties of the COO state. Charge and orbital ordering occurs in this compound below $T_{CO} \sim 220$ K and has been investigated by various techniques.[9,33–36] Magnetic ordering of the CE type occurs below $T_N = 110$ K.[9] Compared to the perovskite manganites, the COO state is exceptionally stable in $La_{1/2}Sr_{3/2}MnO_4$ and only very high fields of the order of 30 T can melt the ordered state, implying negative magnetoresistance effects.[37] Good metallic properties are, however, never achieved in the single-layered manganites $La_{1-x}Sr_{1+x}MnO_4$ neither by magnetic field nor by doping.[38,39]

In a recent work, we have studied the magnetic excitation spectrum of the CE-type ordering in $La_{1/2}Sr_{3/2}MnO_4$ at low temperatures.[20] The analysis of the spin-wave dispersion is fully consistent with the classical charge and orbital order model[12] and underlines the dominant character of the FM intrachain interaction: The magnetic structure has to be regarded as a weak AFM coupling of stable FM zigzag elements. In this paper, we address the thermal evolution of the CE magnetic ground state and report on the development of the static and dynamic magnetic correlations as studied in neutron scattering experiments and in macroscopic measurements: The magnons of the static CE order transform into anisotropic short-range magnetic correlations remaining clearly observable for $T_N < T < T_{CO}$. Here, magnetic correlations can be described by a loose AFM coupling of FM zigzag-chain fragments. These CE-type fluctuations compete with isotropic ferromagnetic correlations between T_N and T_{CO}, and they fully disappear upon melting the COO state above T_{CO}. Instead, in the charge and orbital disordered phase above T_{CO}, we find purely FM correlations, which remarkably resemble those observed in the metallic FM phases in cubic manganites.

II. EXPERIMENT

$La_{1/2}Sr_{3/2}MnO_4$ crystallizes in a tetragonal structure of space-group symmetry $I4/mmm$ with room-temperature lattice constants $a = 3.86$ Å and $c = 12.42$ Å.[40] For most of the neutron scattering experiments, we used the same large crystal as for the analysis of the spin-wave dispersion.[20] The thermodynamic measurement and some elastic parts of the neutron scattering experiments were done with a smaller sample. All crystals were grown in an identical way by using the floating-zone technique described in Ref. 41. Elastic neutron scattering experiments were performed at the thermal double-axis diffractometer 3T.1 and at the triple-axis spectrometer G4.3, which are both installed at the Laboratoire Léon Brillouin (LLB) in Saclay. Selected scans measured at the high-flux instrument 3T.1 were repeated with the same neutron energy $E = 14.7$ meV at the G4.3 spectrometer with an energy resolution $\Delta E \lesssim 0.6$ meV to estimate the influence of slow magnetic fluctuations. The double-axis spectrometer integrates over a sizable energy interval, but all data taken on both instruments quantitatively agree very well, which suggest that the diffuse magnetic scattering is associated with time scales longer than $\sim 10^{-11}$ s. Data using polarized neutrons were acquired at the FLEX spectrometer at the Hahn-Meitner Institut in Berlin. Inelastic neutron data were collected on the spectrometers 1T, 2T, and 4F, which are installed at the thermal and cold sources at the LLB and on the cold instrument PANDA at the Forschungsreaktor FRM II in Munich. At all instruments, the (002) Bragg reflection of pyrolytic graphite (PG) was used as a monochromator and to analyze the energy of the scattered neutrons. The energy on the analyzer side was always fixed to $E_f = 14.7$ meV at the thermal instruments and typically to $E_f = 4.66$ meV on the cold machines. To suppress spurious contaminations by second harmonic neutrons, an appropriate filter, either PG or cooled beryllium, was mounted in front of the analyzer. In most of the measurements, the sample was mounted with the tetragonal c axis vertical to the scattering plane, so that scattering vectors $(hk0)$ were accessible. Some data were collected in a different scattering plane defined by the [110] and [001] directions of the tetragonal structure.

Specific-heat measurements were carried out by using a home-build calorimeter working with a "continuous heating" method. Magnetization was measured in a commercial vibrating sample magnetometer and electric resistivity by standard four-contact method.

III. RESULTS

Before starting the discussion of our results, we illustrate the different structural and magnetic superstructures of the COO state with the aid of Fig. 1. Below T_{CO}, the checkerboard arrangement of the nominal Mn^{3+} and Mn^{4+} sites doubles the structural unit cell to lattice spacings $\sqrt{2}a \times \sqrt{2}a$ with $a \sim 3.8$ Å, which is the lattice constant of the original tetragonal cell. The concomitant orbital ordering reduces the symmetry and the nuclear lattice becomes orthorhombic with lattice constants $2\sqrt{2}a$ along [110] and $\sqrt{2}a$ along $[1\bar{1}0]$. The ordering of charges and orbitals is related to superstructure reflections with $\boldsymbol{k}_{CO} = \pm(\frac{1}{2}\frac{1}{2}0)$ and $\boldsymbol{k}_{OO} = \pm(\frac{1}{4}\frac{1}{4}0)$ in diffraction experiments, respectively. We emphasize once more that the interpretation of the superstructure in terms of integer charge and orbital ordering is only qualitative. The analysis of the real structural distortion reveals much smaller effects than expected for an integer charge ordering and still needs quantitative studies and analysis. Considering the magnetic ordering, the CE-type structure can be divided into two sublattices distinguishing between the two magnetic species. For the Mn^{3+} ions, the magnetic unit cell is of the same size as the nuclear one,

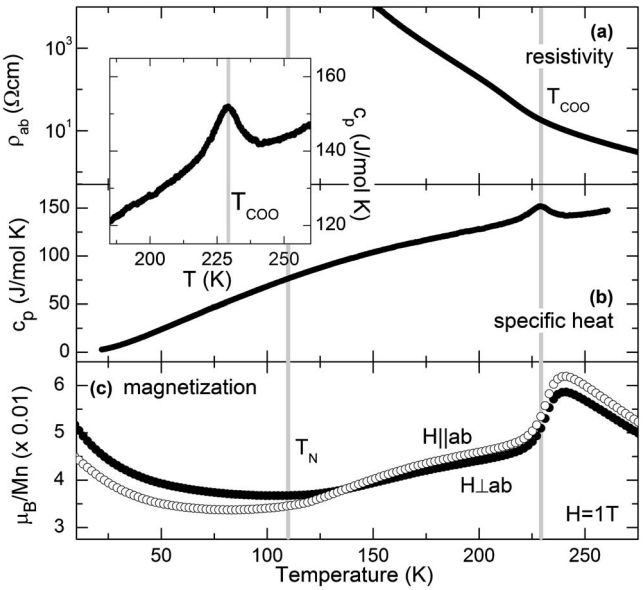

FIG. 2. (a) Temperature dependence of the in-plane electric resistivity ρ_{ab}, (b) the specific heat c_p, and (c) the macroscopic magnetization for a field $H=1$ T applied parallel and perpendicular to the *ab* planes. Vertical gray lines mark T_{CO} and T_N as determined in the neutron scattering experiments.

$\sqrt{2}a \times 2\sqrt{2}a$, but it is rotated by 90° with the long axis along $[1\bar{1}0]$ and propagation vectors $\boldsymbol{k}_{Mn^{3+}} = \pm(\frac{1}{4}\ -\frac{1}{4}\ 0)$. Therefore, the Mn^{3+} spins and the orbital lattice contribute at different $\boldsymbol{Q}$ positions, e.g., there is a magnetic contribution at $\boldsymbol{Q}=(0.75\ 0.25\ 0) \equiv (0.25\ -0.25\ 0)$, but not at $\boldsymbol{Q}=(0.25\ 0.25\ 0)$, where the orbital lattice contributes. The Mn^{4+} spins contribute to neither of these positions, but to positions indexed by $\boldsymbol{k}_{Mn^{4+}} = \pm(\frac{1}{2}00)$ and $\pm(0\frac{1}{2}0)$. The full magnetic cell has to be described in a pseudotetragonal lattice with $2\sqrt{2}a$ along [110] and $[1\bar{1}0]$, as shown in Fig. 1. However, the orthorhombic distortion of the tetragonal symmetry induces a twinning due to the orbital ordering in a sample crystal, as the zigzag chains can either run along [110] (orientation I) or along $[1\bar{1}0]$ (orientation II), and the arrangement described above is superimposed by the same but rotated by 90°. Both twin orientations contribute equally strong in our samples, but for the analysis, we will always refer to orientation I depicted in Fig. 1. We emphasize that the twinning due to the COO orthorhombic distortion is the only one occurring in $La_{1/2}Sr_{3/2}MnO_4$, whereas the octahedron tilt and rotation distortions in the perovskite manganates imply a complex twinning with up to 12 superposed domain orientations.

A. Thermodynamic properties

As a first characterization, we have analyzed the macroscopic properties of our samples that reflect the unusual evolution of the magnetic state as well as the COO ordering. In Fig. 2, we show the temperature dependence of the electric resistivity $\rho_{ab}(T)$ along the planes, the specific heat $c_p(T)$, and the macroscopic *dc* magnetizations $M_\perp(T)$ and $M_\parallel(T)$ for a field $H=1$ T applied perpendicular and parallel to the MnO_2 layers, respectively. All three quantities show a well-defined anomaly, which determines $T_{CO}=227(2)$K, but none around T_N. The electric resistivity ρ_{ab} exhibits insulating behavior with a significant jumplike increase at T_{CO} reflecting the real-space ordering of the charge carriers.[38] Note that we find no hysteresis in the temperature dependence of the resistivity at T_{CO}. The specific heat displays a pronounced anomaly at the same temperature documenting the well-defined character of the COO transition in our $La_{1/2}Sr_{3/2}MnO_4$ crystal. Below T_{CO}, however, the specific heat seems to be determined by phononic contributions, and it is difficult to detect a clear signature for an additional release of entropy around the magnetic ordering, which suggests the formation of short-range magnetic correlations well above T_N.

The macroscopic magnetization $M(T)$ [Fig. 2(c)] is directly correlated with the neutron scattering results (see below). For $T > T_{CO}$, $M(T)$ linearly increases upon cooling and $M_\perp$ is always smaller than $M_\parallel$, which indicates an easy-plane anisotropy parallel to the MnO_2 layers. The magnetization reaches a maximum slightly above T_{CO}, at $T \approx 240$ K, and it is strongly suppressed at the transition into the COO phase. Upon further cooling, $M(T)$ continues to decrease down to $T=90$ K and it roughly scales with the temperature dependence of a diffuse ferromagnetic neutron intensity (see below). Remarkably, there is no well-defined signature of the Néel transition, as $M(T)$ continuously varies across T_N, both for $H \perp ab$ and $H \| ab$. The ratio between $M_\perp$ and $M_\parallel$ agrees with the expectations for an AFM order of moments aligned within the *ab* planes due to an easy-plane anisotropy. Below $T \approx 135$ K, $M_\perp$ is larger than $M_\parallel$, whereas the opposite is observed in the paramagnetic phase. At low temperatures, below $T \approx 50$ K, both magnetization components $M_\perp$ and $M_\parallel$ exhibit a pronounced Curie-type upturn. Usually, a low temperature upturn in the magnetization is associated with sample-dependent impurities, but in the case of $La_{1/2}Sr_{3/2}MnO_4$, it might be a generic feature as observed in various studies using different sample crystals.[38]

The most prominent feature in the magnetic susceptibility concerns the sudden magnetization drop at the COO transition. As pointed out by Moritomo *et al.*,[38] the singular behavior at T_{CO} can be attributed to the quenching of the double-exchange interaction with the localization of the e_g electrons into the charge ordered state, which is supported by electron spin resonance measurements.[42] The neutron analysis, in addition, clearly shows that the FM correlations are not just reduced at T_{CO}, but they become replaced by the AFM CE-type fluctuations even well above the Néel transition. Due to the distinct magnetic symmetries, the magnetic transition from a FM state to the AFM CE-type order must be of first order that allows for phase coexistence.

B. Elastic magnetic scattering

1. Polarized neutron diffraction

In a scattering experiment, the superposition of both twin orientations arising from the COO orthorhombic distortion mixes structural and magnetic contributions at a quarter-

TABLE I. Results of the longitudinal polarization analysis for various magnetic and structural Bragg positions at $T=5$ K. For each $\boldsymbol{Q}$ position, the observed neutron intensity is shown for the different choices of the neutron quantization axis $\boldsymbol{P}_j$, $\boldsymbol{P}\|\boldsymbol{Q}$ (x), $\boldsymbol{P}\perp\boldsymbol{Q}$ and within (y), and $\boldsymbol{P}\perp\boldsymbol{Q}$ and perpendicular to the scattering plane(z), and the spin flipper on (SF) or off (NSF). The last column gives the calculated decomposition of the observed intensity into magnetic and structural components.

$\boldsymbol{Q}$		P_x	P_y	P_z	$I_{\mathrm{mag}}/I_{\mathrm{struc}}$
(0.75 0.25 0)	SF	14511	1087	14619	
	NSF	796	14179	848	1.00/0.00
(0.75 0.75 0)	SF	1625	161	1624	
	NSF	208	1659	264	0.94/0.06
(1.25 0.25 0)	SF	3013	475	3194	
	NSF	486	3085	498	0.91/0.09
(1.75 0.25 0)	SF	8550	4475	7508	
	NSF	72665	76331	72745	0.05/0.95
(0.5 10)	SF	12999	1200	13091	
	NSF	797	12653	734	1.00/0.00
(2 0 0)	SF	2486	1903	1800	
	NSF	30032	30846	31304	0.00/1.00

indexed position. The magnetic contribution of orientation I is superimposed by the orbital contribution of orientation II and vice versa. Both contributions can, however, be well separated by using polarized neutrons. In the classical polarization analysis, spin-flip (SF) scattering is always magnetic, whereas non-spin-flip (NSF) scattering can be either magnetic or structural: Magnetic moments aligned perpendicular to both the scattering vector $\boldsymbol{Q}$ and the neutron's polarization $\boldsymbol{P}$ contribute to the SF channel, while those aligned parallel to $\boldsymbol{P}$ to the NSF channel.[43] Table I summarizes the results of the longitudinal polarization analysis of selected superstructure reflections at $T=5$ K determined at the FLEX spectrometer for three different choices of the neutron quantization axis, $\boldsymbol{P}\|\boldsymbol{Q}$ (x), $\boldsymbol{P}\perp\boldsymbol{Q}$ and within the ab plane (y), and $\boldsymbol{P}\perp\boldsymbol{Q}$ and perpendicular to the ab plane (z). In addition to the quarter-indexed reflections, Table I also includes the half-indexed reflection $\boldsymbol{Q}=(0.5\ 1\ 0)$ and the integer-indexed reflection $\boldsymbol{Q}=(2\ 0\ 0)$. These reflections are entirely magnetic, respectively, nuclear, and serve as reference positions for the analysis of the quarter-indexed reflections, which provide an estimate of the experimental accuracy with flipping ratios $\mathrm{FR}=I^{\mathrm{SF}}:I^{\mathrm{NSF}}$ of the order of 15. Inspecting the distribution of magnetic intensity at $\boldsymbol{Q}=(0.5\ 1\ 0)$ in the various $\boldsymbol{P}_j$ channels immediately clarifies, that the magnetic moments are confined to the ab planes; a canting of the moments out of the planes must be less than $\sim 5°$, which is in good agreement with other estimations.[9] Knowing the experimentally determined FRs, the scattering observed at a quarter-indexed position can be decomposed into magnetic and structural contributions (see the last column of Table I). With increasing $|\boldsymbol{Q}|$, the magnetic scattering is suppressed following the square of the form factor and, simultaneously, the structural component is enhanced. For small $|\boldsymbol{Q}|$, the observed intensity is, however, entirely of magnetic origin, and in the following, we may associate any scattering appearing around $\boldsymbol{Q}=(0.75\ 0.25\ 0)$ with magnetic correlations.

2. Unpolarized neutron diffraction

The thermal evolution of the static magnetic correlations around $\boldsymbol{Q}=(0.75\ 0.25\ 0)$ has been determined in the elastic neutron scattering experiments at the spectrometers 3T.1 and G4.3 at the LLB. Within the estimated experimental energy resolution, "static" refers to magnetic correlations on a time scale longer than $\sim 10^{-11}$ s. In Fig. 3, we show mappings of the reciprocal space around the magnetic CE position $\boldsymbol{Q}_{\mathrm{CE}}=(0.75\ 0.25\ 0)$ including the FM position $\boldsymbol{Q}_{\mathrm{FM}}=(1\ 0\ 0)$ for four different temperatures, which are above T_{CO} in the charge and orbital disordered phases at 250 K, in the COO phase above T_N at 200 and at 150 K and below T_N in the CE-ordered state at 100 K. All four maps exhibit strong magnetic response, and the comparison of the different temperatures directly reveals drastic changes in the character of the magnetic correlations.

In the charge and orbital disordered phase at $T=250$ K [Fig. 3(a)], the magnetic scattering appears as a broad and isotropic feature centered around $\boldsymbol{Q}_{\mathrm{FM}}=(100)$. In the K_2NiF_4-type structure corresponding to space group $I4/mmm$, (1 0 0) is not a three-dimensional Bragg point due to the body-centered stacking of the MnO_2 layers. However, when neglecting any magnetic interlayer coupling, i.e., analyzing magnetic correlations in a single layer, any $(1\ 0\ 0q_l)$ is a two-dimensional Bragg position sensing FM in-plane correlations. From the width of the signal in the $(h\ k\ 0)$ plane, a nearly isotropic in-plane correlation length $\xi_{\mathrm{iso}}\approx 8$ Å can be estimated for ferromagnetic clusters (see below). From the Q_l dependence of the FM signal at $(0\ 0Q_l)$ studied on a slightly underdoped sample,[44] we may deduce the fully two-dimensional nature of the FM scattering and that the moments are predominantly aligned within the planes in accordance with the anisotropy of the magnetic susceptibility.

With the transition into the COO phase, the magnetic correlations abruptly change. At $T=200$ K [Fig. 3(b)], the FM signal around $\boldsymbol{Q}_{\mathrm{FM}}$ has drastically lost intensity, while, simul-

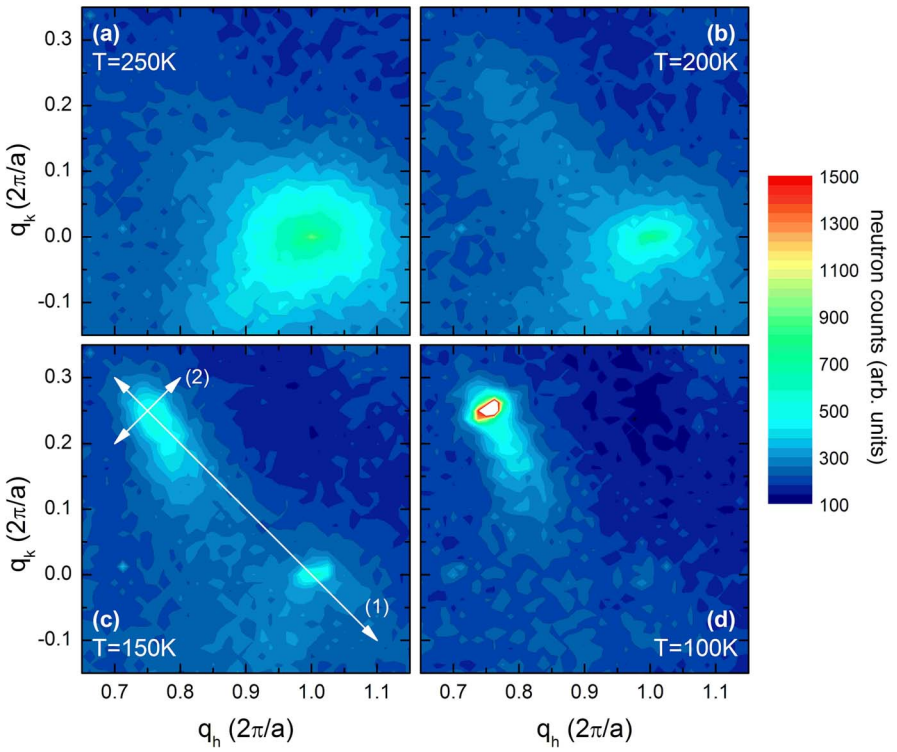

FIG. 3. (Color online) Intensity mappings of the elastic magnetic scattering around the magnetic CE-type position $\boldsymbol{Q}_{\mathrm{mag}}=(0.75\ 0.25\ 0)$ and around the two-dimensional FM zone center (1 0 0) at various temperatures (a) above the charge-orbital ordering at $T=250$ K, [(b) and (c)] below T_{CO} but above the Néel transition at $T=200$ K and $T=150$ K, and (d) below the AFM transition at $T=100$ K. All maps were calculated from a grid of 41×41 data points with $\Delta q_h=\Delta q_k=0.0125$. The two arrows in (c) denote the directions of the scans investigated in more detail; scan (1) senses the stacking of zigzag fragments in the CE phase and scan (2) their length.

taneously, magnetic intensity is increased along the path $(100)\rightarrow(0.75\ 0.25\ 0)$. Upon further cooling, intensity is transferred from $\boldsymbol{Q}_{\mathrm{FM}}$ to the quarter-indexed position $\boldsymbol{Q}_{\mathrm{CE}}=(0.75\ 0.25\ 0)$, and at $T=150$ K, two separate features are well distinguished in the mapping [Fig. 3(c)]. The transition into the CE phase at T_N finally completely suppresses the FM response and at 100 K, all magnetic scattering is centered at the magnetic CE-type Bragg reflection $\boldsymbol{Q}_{\mathrm{CE}}$ [Fig. 3(d)].

To further analyze the competition between FM- and CE-type correlations, we studied the temperature dependence along the two lines depicted in Fig. 3(c) in more detail. Scan 1 runs along $[1\bar{1}0]$ and connects $\boldsymbol{Q}_{\mathrm{FM}}$ and $\boldsymbol{Q}_{\mathrm{CE}}$, while scan 2 is oriented perpendicular along [110] and crosses scan 1 at $\boldsymbol{Q}_{\mathrm{CE}}$. As around $\boldsymbol{Q}_{\mathrm{CE}}$, only the magnetic scattering of the twin orientation with the zigzag chains running along [110] contributes (orientation I); scan 1 probes the magnetic correlations perpendicular to the chains, i.e., the stacking of the FM zigzag chains within the MnO_2 planes. In contrast, scan 2 determines the correlations parallel to the chains.

Let us start with the discussion of the thermal evolution of the magnetic scattering along scan 1 (see Fig. 4). At the highest temperature investigated, $T=250$ K, the spectrum consists of a broad, Lorentzian-shaped feature centered at $\boldsymbol{Q}_{\mathrm{FM}}=(1\ 0\ 0)$, as is already evident in Fig. 3(a). This signal is due to ferromagnetic planar correlations of limited correlation length. With decreasing temperature, the signal roughly stays unaffected until charge and orbital ordering sets in at $T_{\mathrm{CO}}\approx227$ K. Below T_{CO}, the signal at $\boldsymbol{Q}_{\mathrm{FM}}$ looses spectral weight and additional weak and very broad features become apparent around $(1\mp\varepsilon,\pm\varepsilon,0)$. The latter features continuously sharpen, gain in intensity, and shift outward until they finally lock into the commensurate CE-type positions with $\varepsilon=\pm0.25$ close to $T_N\approx110$ K. Within the magnetically ordered phase below T_N, we do not find any evidence for FM correlations anymore and the AFM CE-type reflections become sharp and resolution limited at low temperature [Fig. 4(b)].

The thermal evolution along scan 2, i.e., along [110] and parallel to the zigzag chains, is shown in Fig. 5. At $T=250$ K, no signal is observable at $\boldsymbol{Q}_{\mathrm{CE}}$. However, below the COO transition, a magnetic signal emerges, which is easily separated from the background level already at 220 K, i.e., more than 100 K above T_N. Note that there is no structural component in the scattering at these $|\boldsymbol{Q}|$ values (see above). The magnetic signal at $\boldsymbol{Q}_{\mathrm{CE}}$ rapidly sharpens and increases in intensity, which reflects the transfer of spectral weight from $\boldsymbol{Q}_{\mathrm{FM}}$ along the path $(1\ 0\ 0)\rightarrow(0.75\ 0.25\ 0)$ to $\boldsymbol{Q}_{\mathrm{CE}}$. The magnetic phase transition at T_N is evidenced by the change in the line shape: Below 110 K, the profile changes from a broadened Lorentzian reflecting the finite correlation length into a resolution-limited Gaussian reminiscent of long-range magnetic order. The intensity of the reflection monotonically increases down to the lowest temperature investigated, $T=3$ K.

So far, we have only discussed the magnetic correlations within the MnO_2 layers. In Fig. 6, we show raw-data scans along $\boldsymbol{Q}=(0.25\ 0.25q_l)$ for various temperatures below T_{CO} aiming at the magnetic correlations along [001]. In contrast to the in-plane correlations, the scans along [001] are not structured above T_N. The CE-type magnetic correlations are entirely two dimensions for $T>T_N$, which are similar to many other layered magnets with the same K_2NiF_4 structure type.[45] Below the magnetic phase transition at T_N, a well-defined structure develops along q_l, and two distinct sets of reflections centered around half- and integer-indexed q_l values are detected. Both types of reflections can be associated with a different stacking along the c axis, and the observed

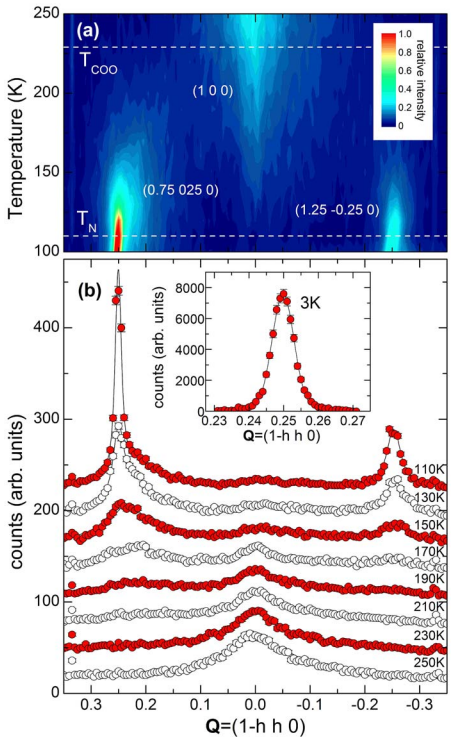

FIG. 4. (Color online) Temperature dependence of the elastic magnetic intensity along scan 1, which is perpendicular to the zigzag chains. (a) Contour plot derived from a grid of data with $\Delta T = 10$ K and $\Delta q_k = 0.005 \frac{2\pi}{a}$. (b) Representative raw-data scans underlying the contour plot. For clarity, the data are successively shifted vertically by 300 counts. The inset gives the profile of the magnetic Bragg reflection at low temperatures, $T = 2.5$ K. Lines correspond to fits as described in the text. In all data, a minor contamination by second harmonic neutrons centered at $\boldsymbol{Q} = (1\ 0\ 0)$ is subtracted. The different scatterings of the two CE-type reflections arise from the Mn form-factor and geometry conditions.

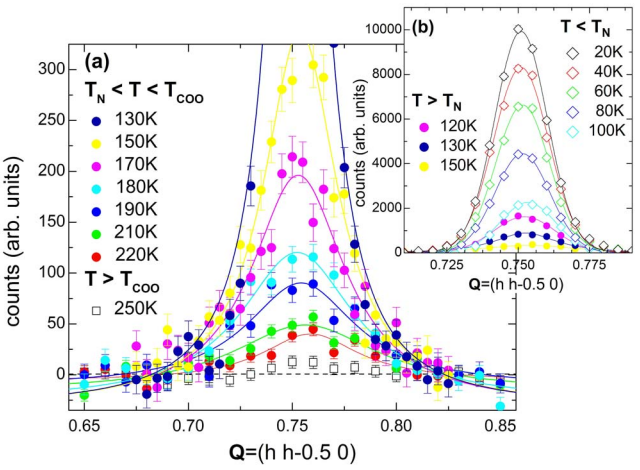

FIG. 5. (Color online) Temperature dependence of the elastic magnetic intensity along scan 2, which is parallel to the zigzag chains, at selected temperatures (a) above and (b) below the Néel transition at $T_N = 110$ K. Note that for the scans at 150 and 130 K, the scale on the ordinate is the same in both panels. In all data, a common background is subtracted. Lines correspond to fits with either Lorentzians (folded with the resolution) or resolution-limited Gaussians as discussed in the text.

distribution of intensity with the half-indexed q_l values dominating agrees well with former observations.[9,39] Along [001], the profile of the reflections is always significantly broader than the experimental resolution, which indicates a finite correlation length perpendicular to the layers of about 50 Å even at lowest temperatures. In order to estimate the correlation lengths reflecting an exponential decay of the order parameter, $\exp(-\frac{q_i}{\xi_i})$, we always fit the measured profile by a Lorentzian, with half width at half maximum $\kappa_i = \frac{1}{\xi_i}$, which is folded with the experimental resolution. At a usual phase transition, one expects the critical Lorentzian-shaped scattering to transform into sharp peaks described by the Gaussian resolution function.

For a quantitative analysis of the diffuse magnetic scattering, we modeled all spectra assuming resolution folded Lorentzian or, at lower temperatures, Gaussian line shapes for the different contributions. The integrated intensity of the reflection then directly determines the square of the magnetic order parameter, and the width, which is corrected for resolution effects, yields the inverse of the magnetic correlation length. The results of this analysis are summarized in Fig. 7. Structural superlattice reflections probing the order parameter of the orbital and the charge ordering, which set the frame for the discussion of the magnetic correlations, appear below T_{CO}, which are in good agreement with the literature.[33,35,36] The temperature dependencies of the intensity of the FM scattering at $\boldsymbol{Q}_{FM} = (1\ 0\ 0)$ and that of the CE-type reflection $\boldsymbol{Q}_{CE} = (0.75\ 0.25\ 0)$ as determined from the scans presented in Figs. 4 and 5 are shown in Figs. 7(a)–7(c). With the transition into the COO phase at T_{CO}, the intensity of the FM correlations decreases and vanishes close to T_N. The in-plane correlation length of the FM signal is isotropic and temperature independent, $\xi_{iso} \approx 8$ Å. Below

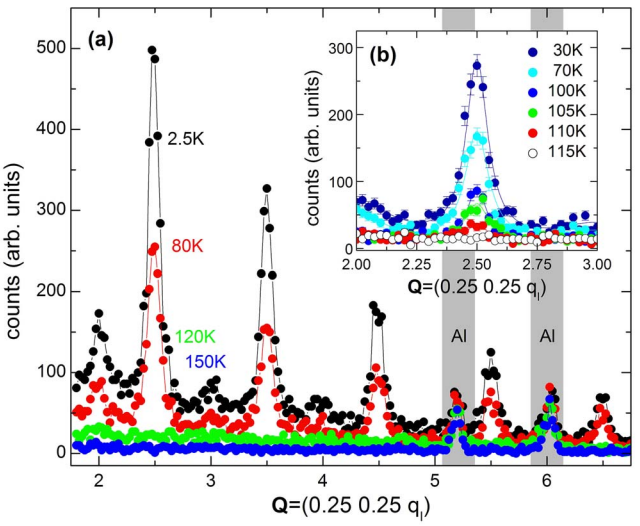

FIG. 6. (Color online) (a) Raw-data scans along the line (0.25 0.25 q_l) for various temperatures below T_{CO}. Gray-shaded areas mark spurious contributions by the scattering from aluminum. (b) Raw-data scans along [0 0 1] centered around $q_l = 2.5$ for various temperatures close to T_N. Lines denote fits with Lorentzians.

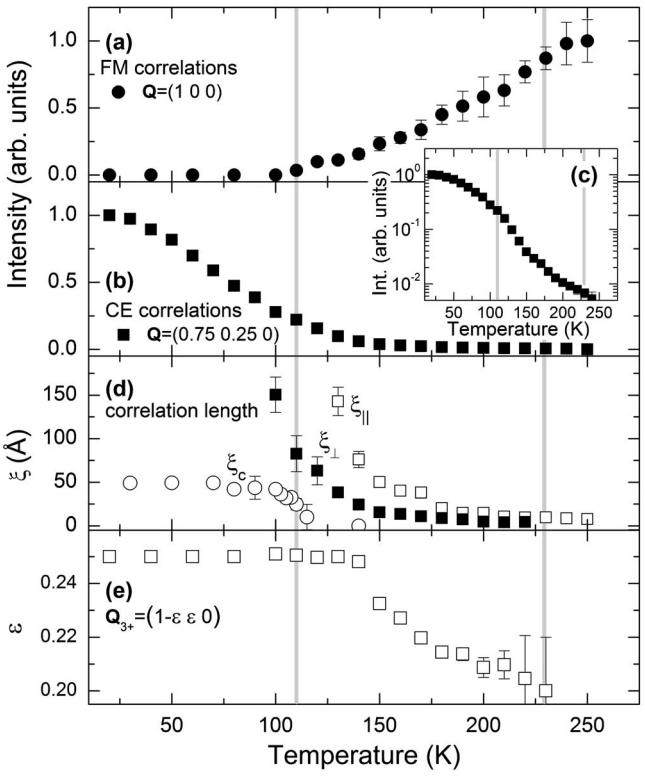

FIG. 7. Summary of the results of the analysis of the elastic magnetic scattering showing the temperature dependence of (a) the intensity observed at the FM position $\boldsymbol{Q}=(1\ 0\ 0)$ and [(b) and (c)] at the AFM position $\boldsymbol{Q}=(0.75\ 0.25\ 0)$ on a linear and logarithmic scale (d) of the determined correlation length ξ in a direction parallel to the chains $\xi_{\|}$, perpendicular to the chains, and within the *ab* plane, $\xi_{\perp}$, and along the tetragonal axis ξ_c, and (e) of the position of the AFM signal along the line $\boldsymbol{Q}=(1\mp\varepsilon\pm\varepsilon 0)$.

T_N, no FM signal can be detected anymore in our neutron scattering experiments. In contrast, the AFM correlations of the CE type emerge with the transition into the COO phase and compete with the FM phases between T_{CO} and T_N.

The observed peak height of the magnetic scattering at the CE-type Bragg reflection does not exhibit a clear anomaly at T_N and the thermal evolution appears continuous in the entire temperature regime below 225 K, although the major intensity increase is found below T_N. The temperature dependence of the magnetic reflections, for example, (0.5,1,0), sensing the magnetic order of the Mn^{4+} sites perfectly scales with that of the quarter-indexed ones sensing the Mn^{3+} order confirming the close coupling of the two magnetic sublattices forming the complex CE-type magnetic ordering. A clear indication for the magnetic phase transition at T_N is, however, seen in the behavior of the magnetic correlation lengths [Fig. 7(d)]. The AFM correlations of the CE type exhibit a pronounced anisotropy and temperature dependence. Both in-plane correlation lengths, $\xi_{\|}$ parallel and $\xi_{\perp}$ perpendicular to the zigzag chains, rapidly increase and finally diverge as the temperature decreases toward $T_N\approx 110$ K. For $T>T_N$, $\xi_{\|}$ is always larger than $\xi_{\perp}$, which indicates that the intrachain correlations are much better defined than the interchain correlations. Close to T_N, the ratio between $\xi_{\|}$ and $\xi_{\perp}$ is most pronounced attaining a factor of ~ 4 and $\xi_{\|}$ diverges at slightly higher temperatures than $\xi_{\perp}$. The out-of-plane correlation length for the CE ordering, ξ_c, is also included in Fig. 7(d). In contrast to the in-plane correlations, ξ_c remains finite at lowest temperatures, $\xi_c\approx 50$ Å, and the interlayer correlation rapidly disappears above T_N. Finally, Fig. 7(e) displays the evolution of the AFM peak position along the line $(1\mp\varepsilon,\pm\varepsilon,0)$. The incommensurability ε directly reflects the AFM coupling between adjacent or more distant zigzag chains. With the onset of the magnetic correlations near T_{CO}, ε monotonically increases and locks little above T_N into the commensurate value $\varepsilon=0.25$. Hence, the modulation wavelength perpendicular to the zigzag chains decreases upon cooling until at T_N adjacent chains antiferromagnetically couple. The asymmetric shape of the CE-type diffuse scattering close to T_N [see, e.g., Fig. 4(b)] has to be ascribed to the asymmetric distribution of $\varepsilon\leq 0.25$: The stacking of the zigzag chains cannot occur with a repetition scheme shorter than nearest-neighbor chains, which is $2\sqrt{2}a$ corresponding to $\varepsilon=0.25$.

We emphasize that the well-defined three-dimensional magnetic CE-type order, together with the full suppression of the FM response, is reminiscent of the high quality of our crystals. An earlier sample of $La_{1/2}Sr_{3/2}MnO_4$ (Ref. 44) as well as the crystal used in Ref. 9 exhibit significantly reduced CE-type correlation lengths. The high quality of the sample is further documented by a clear specific-heat anomaly observed at T_{CO} (see below).

C. Dynamic magnetic correlations

So far, we have only considered the thermal evolution of the static magnetic correlations. The anisotropic character of the AFM correlation and the competition between AFM and FM interactions should, however, also significantly influence the dynamic magnetic properties. The development of the magnetic correlations at finite-energy transfer has been studied in the experiments at the spectrometers 4F, 1T, 2T, and PANDA.

In our previous work,[20] we established the low-energy part of the magnetic excitations in the CE-type ordered state, which can be well described by spin-wave theory. At low temperatures, the magnon dispersion is anisotropic with a steep dispersion along the zigzag chains, which reflects the dominant FM interaction along this direction.[20] The pronounced magnon anisotropy can be taken as a strong indication against the bond-centered dimer model, whereas it is naturally described within the CE-type orbital and magnetic model (for details, see Ref. 20).

In the CE-ordered phase at $T=5$ K, the spin-wave spectrum is gaped at the antiferromagnetic zone center, $\boldsymbol{q}=0$ [see Fig. 8(a)], and two distinct magnon contributions can be resolved. The degeneracy of the two AFM magnon branches seems to be removed due to anisotropy terms. As already seen in the high-temperature behavior of $M(T)$, $La_{1/2}Sr_{3/2}MnO_4$ exhibits an easy-plane single-ion anisotropy above the COO transition. Due to the orthorhombic symmetry in the COO phase, the easy-plane anisotropy[46] must transform into an easy-axis symmetry, which is hidden by the twinning in the macroscopic measurements. The magnetic

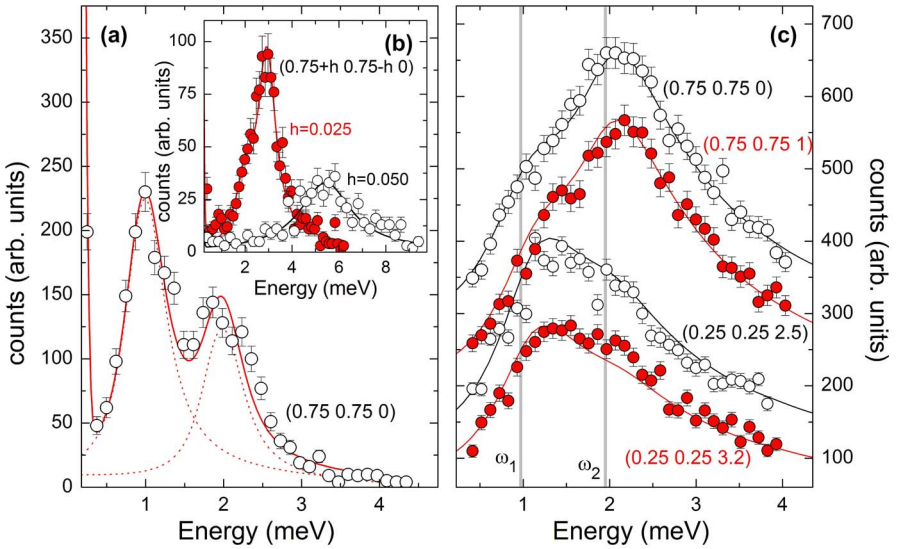

FIG. 8. (Color online) (a) Energy scan at the AFM zone center $\boldsymbol{Q}=(0.75\ 0.25\ 0)$ at $T=4$ K and (b) at different positions perpendicular to the propagation of the chains at $\boldsymbol{Q}=(0.75+q_h\ 0.75-q_h\ 0)$. (c) q_l dependence of the magnon signal taken with a different experimental setup. Lines denote fits to the data. See text for details.

anisotropy, however, is visible in the excitation spectra in the form of the observed zone-center gap and splitting. At the antiferromagnetic zone center, we find two magnon excitations around 1.0 and 2.0 meV [Fig. 8(a)]. The splitting of the modes is, however, restricted to the zone center, and for finite momentum $|\boldsymbol{q}|$, both modes rapidly merge into a single excitation [Fig. 8(b)].

To probe the character of the two zone-center modes, we studied their q_l dependence [Fig. 8(c)]. As only the component of the magnetization perpendicular to the scattering vector contributes in neutron scattering, increasing q_l will suppress a fluctuation polarized along the c axis, while a mode fluctuating perpendicular to c will remain less affected or even increase in intensity. For this purpose, we used a scattering plane defined by [110]/[001], where the steep T_N branch of the dispersion points along the vertical axis. As the vertical $\boldsymbol{Q}$ resolution is low on a focusing triple-axis spectrometer, this configuration integrates over a sizable part of the vertical dispersion strongly affecting the shape of the measured signal. In the scans taken using this configuration [Fig. 8(c)], the two magnon contributions appear only as a rather broad feature, while they can be easily separated with the usual configuration with c vertical to the scattering plane. Due to the weak interlayer coupling, the dispersion along c is negligible and hence the integration is very efficient with [001] vertical. To take the different experimental conditions into account and to resolve the two different magnon contributions in all scans, we convoluted the four-dimensional resolution function with the dispersion surface as derived in Ref. 20 by using the RESLIB code.[47] In a first step, we evaluated the data taken with [001] vertical and refined the magnon energies at $\boldsymbol{q}=0$ yielding $\omega_1=0.97(2)$ meV and $\omega_2=1.97(4)$ meV, respectively. By using these values as a starting point, we modeled the data taken in the second setup. As a first result, all data with different q_l values can simultaneously be described using the same magnon frequencies. There is no measurable spin-wave dispersion vertical to the MnO_2 layers. Like the two-dimensional magnetic scattering above T_N, this behavior fully agrees with that found in numerous layered magnets with the same K_2NiF_4 structure type. Even in the two-dimensional Heisenberg model, a very small interlayer coupling is sufficient to induce three-dimensional magnetic order as the interlayer coupling enters the formula describing the T_N logarithmically.[45] As a second fit parameter, we modeled the intensity distribution at the various q_l positions. With increasing $|\boldsymbol{Q}|$, the signal ω_1 follows the square of the magnetic form factor, while the signal ω_2 is additionally suppressed. Assuming the mode ω_2 to be entirely polarized along c, we find a good agreement with the data, and the splitting of the magnon frequencies can be fully ascribed to different magnetic anisotropies: Fluctuations within the MnO_2 layers are more favorable than those along the c axis as is expected. The sizable gap associated with the in-plane anisotropy, $\omega_1=0.97$ meV, is remarkable as it documents that magnetic moments are also pinned through the orbital anisotropy of the zigzag chains.

To determine the temperature dependence of the magnetic fluctuations, we scanned the excitations around $\boldsymbol{Q}_{CE}=(0.75-0.75\ 0)$ and $\boldsymbol{Q}_{FM}=(1\ 0\ 0)$ in different directions at a constant energy of $E=2.75$ meV. These scans were performed at 10 and 100 K in the CE-ordered phase, in the COO phase above T_N at 130 and at 200 K, and in the disordered phase at 250 K (see Fig. 9). First, we discuss the thermal evolution around $\boldsymbol{Q}_{CE}$. At $T=10$ K and along [110], i.e., parallel to the zigzag chains, the spectrum can be decomposed into the two magnon contributions centered at $\boldsymbol{Q}_{CE}+\boldsymbol{q}$ and $\boldsymbol{Q}_{CE}-\boldsymbol{q}$ [see Fig. 9(a)]. However, as the dispersion in this direction is steep, both signals strongly overlap in agreement with our previous study.[20] With increasing temperature, the magnon signal is suppressed roughly following the magnetic order parameter and shifts outward due to the overall softening of the magnetic dispersion. In consequence, the magnon contributions are fully resolved at $T=100$ K, which is corroborated by further scans at 4 meV exhibiting a similar behavior (data not shown). Upon heating across T_N, the inelastic response broadens, but we do not observe a significant change in the magnon frequencies. At 200 K, the spectrum can be described by two contributions centered at the same positions at 100 K, which is indicative of the stable FM interaction within the zigzag-chain fragments. In the perpen-

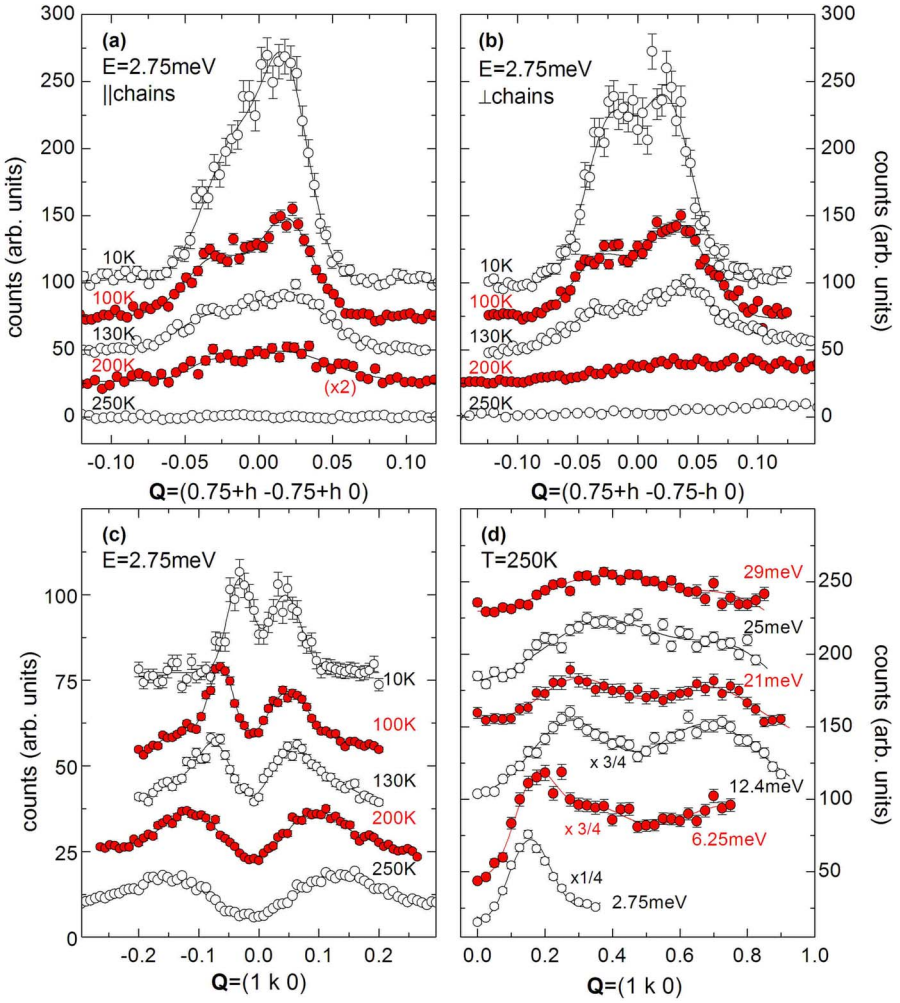

FIG. 9. (Color online) (Upper panel) $\boldsymbol{Q}$ scans at a finite energy $E=2.75$ meV for different temperatures across the CE position (0.75–0.75 0) in a direction (a) parallel to the zigzag chain [1 1 0] and (b) perpendicular to the chains along [1 $\bar{1}$ 0]. (Lower panel) Raw-data scans tracking (c) the temperature dependence of the magnetic fluctuations around the FM position $\boldsymbol{Q}_{\mathrm{FM}}=(1\ 0\ 0)$ with $E=2.75$ meV and (d) the $\boldsymbol{q}$ dependence of the FM fluctuations for $T=250$ K. All scans are corrected for the different Bose contributions after the subtraction of a linear background. For clarity, subsequent scans are shifted by a constant amount on the abscissa. Lines correspond to fits with Gaussians.

dicular direction [Fig. 9(b)], the two magnon contributions are separated already at 10 K, as in this direction the spin-wave velocity is significantly reduced.[20] Upon heating, the signal shifts outward, too, but this shift is more pronounced than that parallel to the chains. Furthermore, for $T>T_N$, the inelastic intensity is fully smeared out, and at $T=200$ K, we do not find any correlations that can be associated with the interzigzag coupling, whereas, in the direction along the chains, the inelastic intensity is still well centered around $\boldsymbol{Q}_{\mathrm{CE}}$. The inelastic CE-type magnetic correlations are thus turning one dimension in character between T_N and T_{CO}: Only the magnetic coupling within a zigzag fragment remains finite close to T_{CO}. Above the charge-orbital ordering, the magnetic fluctuations reminiscent of the CE-type magnetic order are completely suppressed.

Around the FM $\boldsymbol{Q}$ point, we find a fundamentally different behavior of the magnetic fluctuations. $\boldsymbol{Q}_{\mathrm{FM}}=(100)$ is also a zone center of the CE-type magnetic structure, and therefore inelastic neutron scattering may detect the CE-type finite-energy spin-wave modes also around (1 0 0) but with a strongly reduced structure factor (see Fig. 4 in Ref. 20). However, the scattering around (1 0 0) does not evolve like the CE-order parameter and the associated fluctuations described above. The inelastic intensity close to (1 0 0) remains well defined over the entire temperature range up to highest temperatures [see Fig. 9(c)]. At $T=250$ K, the differences between the spectra around the different $\boldsymbol{Q}$ positions are most evident: Around $\boldsymbol{Q}_{\mathrm{CE}}$ no inelastic signal can be detected anymore, whereas the dynamic correlations around $\boldsymbol{Q}_{\mathrm{FM}}$ are clearly structured. These fluctuations are entirely FM in character—there is no evidence for CE-type correlations left at this temperature—and they have to be associated with the isotropic FM clusters revealed in the diffuse magnetic scattering. As around $\boldsymbol{Q}_{\mathrm{FM}}$, both types of magnetic correlations may contribute at finite energy, CE type as well as FM ones; the thermal progression of the dynamics around this position (Fig. 9) documents how the isotropic FM correlations compete with and finally are replaced by the CE-type ordering (upon cooling), as is fully consistent with the coexistence of different magnetic phases in the elastic scattering.

At $T=250$ K, i.e., above any magnetic and charge ordering, we followed the $\boldsymbol{q}$ dependence of the FM fluctuations up to a maximal energy of 35 meV along the main symmetry directions in the MnO_2 layers [see Fig. 9(d)]. The inelastic response is always rather broad in $\boldsymbol{Q}$ space, and above 12.5 meV, two different features strongly overlap, which are, however, centered at equivalent $\boldsymbol{q}$ positions in neighboring FM Brillouin zones, (100) and (110). With increasing energy, both signals disperse toward the FM zone boundary, which they finally reach close to 30 meV at (1 0.5 0). In the diag-

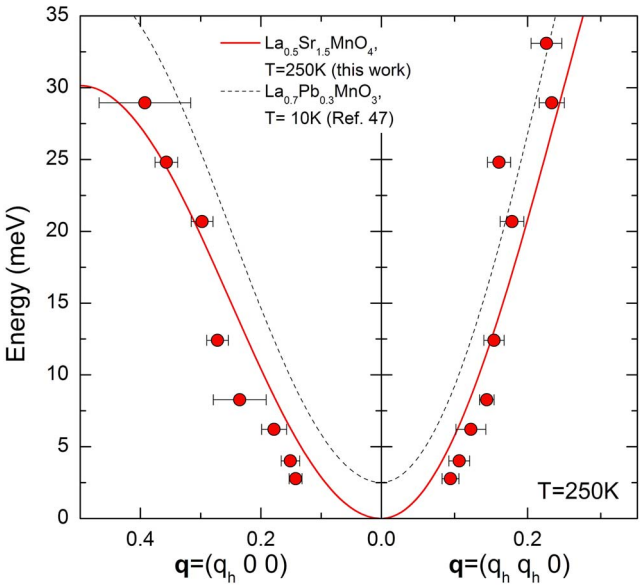

FIG. 10. (Color online) $\boldsymbol{q}$ dependence of the FM fluctuations in the disordered phase at $T=250$ K for $\boldsymbol{q}=(q_h\ 0\ 0)$ and $\boldsymbol{q}=(q_h\ q_h\ 0)$. Solid lines denote a fit to the data using an isotropic dispersion relation according to Eq. (1); dotted lines give the magnon dispersion in the FM metallic state ($T=10$ K) of the perovskite $La_{0.7}Pb_{0.3}MnO_3$ taken from Ref. 48.

onal direction along [110], the energies of the FM fluctuation extend to even higher energies (raw data not shown), and the resulting dispersion of the FM fluctuations in the disordered phase above the COO transition is summarized in Fig. 10.

On a square lattice, the spin-wave dispersion for a Heisenberg ferromagnet with isotropic exchange J_{iso} between nearest neighbors is given by

$$\hbar\omega(\boldsymbol{q}) = 4J_{iso}S[2-\cos(2\pi q_h)-\cos(2\pi q_k)]. \qquad (1)$$

The observed $\boldsymbol{q}$ dependence of the magnetic correlations is reasonably well described by this simple Hamiltonian with only a single nearest-neighbor interaction, which underlines the isotropic character of the FM correlations above T_{CO}. The slight overestimation of the frequencies at the low-$|\boldsymbol{q}|$ limit may arise from the finite size of the FM clusters. We do not find evidence for an excitation gap, and the best fit to the data yields an exchange energy $2J_{iso}S=7.5(5)$ meV. The strength of the ferromagnetic exchange in the disordered phase is significantly reduced compared to the FM interaction in the CE structure, $2J_{FM}S\approx 18$ meV along the zigzag chains,[20] but still points to a sizable hopping mediated through the Zener double exchange even though the single-layer compound remains insulating. The dispersion of the FM correlations above T_{CO} may also be compared to the two nearly half-doped cubic perovskite manganates, $Pr_{0.5}Ca_{0.5}MnO_3$ and $Nd_{0.45}Sr_{0.55}MnO_3$, which exhibit the *A*-type magnetic order corresponding to an AFM stacking of FM layers. These FM layers are fully comparable to the isolated layers in $La_{1/2}Sr_{3/2}MnO_4$. The magnon dispersion in the two perovskite materials is described with $2J_{iso}S=9.04$ meV [$Pr_{0.5}Ca_{0.5}MnO_3$ (Ref. 49)] and $2J_{iso}S=8.15$ meV [$Nd_{0.45}Sr_{0.55}MnO_3$ (Ref. 50)], respectively. Apparently, this FM coupling is a generic feature of the single manganate layers at half doping as long as charge and orbital orderings are suppressed.

Furthermore, $2J_{iso}$ in the COO disordered phase in $La_{1/2}Sr_{3/2}MnO_4$ is well comparable to the magnetic exchange interaction in the FM metallic phases of perovskite manganites: The spin-wave dispersion in the FM phase of the CMR-compound $La_{0.7}Pb_{0.3}MnO_3$ is included in Fig. 10, which is also described by a single nearest-neighbor exchange interaction.[48] The dispersion of magnetic correlations in paramagnetic $La_{1/2}Sr_{3/2}MnO_4$ and the magnon dispersion in FM $La_{0.7}Pb_{0.3}MnO_3$ are remarkably similar. Therefore, the strength of the Zener exchange in the disordered phase above the COO transition in the insulating compound $La_{1/2}Sr_{3/2}MnO_4$ must be of similar magnitude as that in the metallic state of the perovskite CMR compounds.[51] The fact that the dispersion is perfectly isotropic parallel to the planes fully excludes the interpretation that the FM clusters are formed by the coupling of FM zigzag-chain fragments.

IV. COMPARATIVE DISCUSSION OF THE TEMPERATURE DEPENDENCIES OF THE MAGNETIC CORRELATIONS

The combination of the macroscopic and of the neutron scattering studies results in a comprehensive description of the evolution of the magnetic correlations in $La_{1/2}Sr_{3/2}MnO_4$ upon heating across the magnetic and the charge and orbital transition temperatures. The untwinned nature of the $La_{1/2}Sr_{3/2}MnO_4$-sample crystal—besides the twinning directly introduced through the COO order—is of great advantage, as we may easily interpret the distinct signals. Real-space sketches of the magnetic correlations for different temperatures are presented in Fig. 11 to illustrate the different stages of the magnetic ordering between the short-range FM clusters at high temperature and the well-defined CE-type magnetic order at low temperature. In the following, we will discuss the evolution of the magnetic order with increasing temperature. Although the details of the magnetic ordering might depend on the precise composition of the half-doped manganite,[52] and in particular on its single-layer, double-layer, or perovskite structure, the general aspects, how magnetic correlations evolve with temperature, should be qualitatively the same, as previous less comprehensive studies indicate.[53–58]

At low temperature, $La_{1/2}Sr_{3/2}MnO_4$ exhibits the well-established CE-type magnetic order[9] with no trace of another coexisting magnetic phase [see Fig. 11(a)]. Moreover, the magnon excitations in this phase can be well described within spin-wave theory and perfectly agree with the site-centered charge-orbital ordering model. In $La_{1/2}Sr_{3/2}MnO_4$, the spin-wave velocity is highly anisotropic as the magnetic interactions along the zigzag chains are by far the strongest.[20] The localized electron on the Mn^{3+} site seems to yield a strong magnetic bridging within the zigzag chains, as discussed by Solovyev.[31,32]

The magnetic transition at T_N is uncommon, as one does not find any signature of it in the temperature dependence of the magnetization in $La_{1/2}Sr_{3/2}MnO_4$ as well as in many half-doped perovskite manganites.[53–58] The smooth variation of

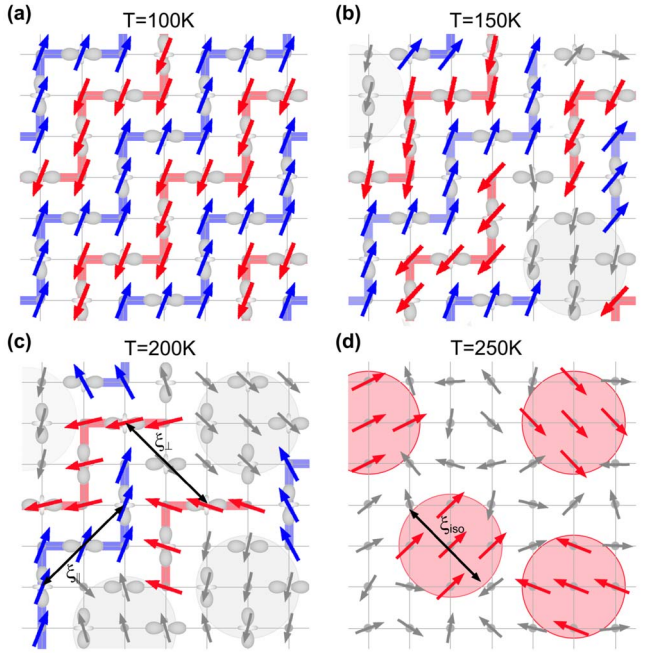

FIG. 11. (Color online) Real-space sketches of the magnetic correlations in the MnO_2 layers for various temperatures (a) in the long-range ordered phase below T_N, [(b) and (c)] in the paramagnetic, but orbital ordered state $T_N < T < T_{CO}$, and (d) in the disordered regime above T_{CO}. Qualitatively, the four sketches are correlated with the intensity mappings presented in Fig. 3, as indicated by the temperatures associated with each sketch.

the susceptibility across T_N relates to the temperature dependence of the magnetic diffuse scattering. Short-range magnetic correlations of the CE type persist above $T_N = 110$ K and can be observed up to T_{CO}. These correlations are purely two-dimensional and restricted to single MnO_2 layers. Moreover, the rodlike structure of the magnetic scattering within the a^*b^* planes documents the strong anisotropy of these two-dimensional correlations: The coupling parallel to the chains reflected by $\xi_\parallel$ is considerably better defined than that in the perpendicular direction $\xi_\perp$, which is in perfect agreement with the magnetic interaction parameters deduced from the spin-wave dipersion.[20] For $T_N < T < T_{CO}$, zigzag fragments are formed as isolated objects [see Figs. 11(b) and 11(c)]. With the reduction in temperature down toward T_N, the typical length $\xi_\parallel$ of the zigzag fragments grows and interchain correlations begin to develop on a length scale $\xi_\perp$, thereby adapting more and more Mn spins into the CE-type correlated matrix [Fig. 11(c)]. All zigzag elements finally order at T_N and the long-range CE-type ordering establishes in the MnO_2 layers [Fig. 11(a)]. Perfect three-dimensional ordering is, however, not achieved and the correlation length perpendicular to the planes remains finite.

The magnetic transition at T_N has thus to be considered as the coherent ordering of preformed FM zigzag-chain fragments into the two-dimensional CE-type structure. In this sense, the AFM transition may be considered as an order-disorder one that explains the lack of a clear anomaly in the magnetic susceptibility.[32] A recent neutron scattering study on the related material, $Pr_{0.55}(Ca_{0.8}Sr_{0.2})_{0.45}MnO_3$, has revealed similar features in the short-range magnetic correlations. Ye *et al.*[58] report on anisotropic magnetic correlations above T_N, which are interpreted in terms of an electronically smecticlike phase. An unusual thermal evolution of the magnetic order across T_N seems to be a characteristic feature of the CE-type ordering.

The picture of preformed FM zigzag fragments is furthermore supported by the thermal evolution of the inelastic magnetic fluctuations, which above T_N exhibit similar anisotropies as the static diffuse scattering. Furthermore, the softening of the magnon frequencies parallel to the chains is less pronounced than that perpendicular to the chains, once more demonstrating the predominance of the FM coupling along the chains within the COO state.[20]

In between the magnetic transition at T_N and charge-orbital ordering at T_{CO}, we find a coexistence of the CE-type and FM elastic correlations documenting how ferromagnetism and the CE-type order compete at these intermediate temperatures. With increasing temperature and approaching T_{CO}, the FM correlations get more and more weight, as is indicated in the sketches in Figs. 11(b) and 11(c). It is remarkable that even in this pure half-doped material with an apparently very stable charge-orbital order, FM and CE-type elastic correlations coexist over a wide temperature interval. This behavior points to microscopic phase separation.[2,3,5,6] We may, however, not fully exclude that the coexistence of CE-type and FM scattering is caused by a canting or a rotation of the spins within a single magnetic cluster, but the different $\boldsymbol{Q}$ shapes of the scattering as well as the different temperature dependencies of the associated correlation lengths render such an explanation unlikely.

In the disordered phase above T_{CO}, the CE-type elastic and inelastic magnetic correlations are fully suppressed. This behavior strongly contrasts with observations in cuprates or nickelates where magnetic correlations reminiscent of stripe order persist far into the charge disordered phases.[59–66] One has to conclude that, at the charge and orbital order transition at T_{CO}, not only the long-range order disappears but also the dynamic COO fluctuations become suppressed. This might be the consequence of the first order character of the charge and orbital order transition in $La_{1/2}Sr_{3/2}MnO_4$, which is already imposed by symmetry. Although our results clearly indicate that the dynamic fluctuations of the CE-type-associated charge-orbital order depicted in Fig. 1 are lost above T_{CO}, we think that some charge and orbital ordering persists on a local scale as is frequently labeled through polaronic effects. Such local electron-lattice coupling should be associated with the strong phonon renormalization observed, e.g., in $La_{0.7}Sr_{0.3}MnO_3$.[67]

In the charge and orbital disordered phase, there is, however, strong diffuse ferromagnetic scattering proving the existence of isotropic FM clusters with an average size of 8 Å [see Fig. 11(d)]. The loosely antiferromagnetically bound FM zigzag-chain fragments seem to transform into these clusters upon heating across T_{CO}. This picture perfectly agrees with the jump in the static susceptibility at T_{CO}. The magnetization of $La_{1/2}Sr_{3/2}MnO_4$ is typical for the CE-type ordering and can be compared to those of other charge ordered perovskite manganites with a narrow one-electron bandwidth.[54,56,57] In addition to the suppression of the

double-exchange interaction due to the charge ordering, the onset of the AFM correlations explains the large drop of $M(T)$ at T_{CO}. The further reduction in $M(T)$ below T_{CO} scales with the decrease in the FM intensity in the diffraction experiments and underlines the competition of FM and CE-type correlations.

The observed sequence of magnetic phases—isotropic short-range ferromagnetic correlations above T_{CO}, anisotropic correlations for $T_N < T < T_{CO}$, and long-range ordering below T_N—is also stabilized in various theoretical approaches.[31,68,69] Based on anisotropic magnetic exchange interactions, Solovyev[31] predicts a magnetically disordered state consisting of stable FM-ordered zigzag elements for $T_N < T < T_{CO}$, just as observed in our neutron data. However, whether or not these magnetic fluctuations are strong enough to stabilize the COO state, as originally proposed in Ref. 31, cannot be finally answered from the present data. However, we emphasize that the CE-type magnetic fluctuations (both elastic and inelastic ones) are very weak slightly below the charge-orbital order shedding some doubt on the interpretation that the magnetic mechanism alone is strong enough to stabilize the charge and orbital ordered state.

V. CONCLUSIONS

In summary, we have studied the magnetic correlations in the charge and orbital ordered manganite $La_{1/2}Sr_{3/2}MnO_4$ by elastic and inelastic neutron scattering techniques and by macroscopic thermodynamic measurements. Besides a simple twinning due to the COO ordering, the real structure of $La_{1/2}Sr_{3/2}MnO_4$ single crystals is simple allowing for a very precise analysis of the diffuse scattering and of the inelastic fluctuations.

The Néel transition in $La_{1/2}Sr_{3/2}MnO_4$ has to be considered as an order-disorder transition of FM zigzag-chain fragments, thereby explaining the absence of well-defined anomalies in the magnetization at T_N, which is characteristic for numerous charge and orbital ordered perovskite materials as well. The in-plane magnetic correlations in $La_{1/2}Sr_{3/2}MnO_4$ are highly anisotropic in character, as the magnetic coupling within the zigzag chains is strongly dominating, whereas adjacent chains are only loosely coupled. FM correlations are fully suppressed below T_N in the CE-type magnetic state in our high-quality crystal of $La_{1/2}Sr_{3/2}MnO_4$, but in between T_N and T_{CO} AFM CE-type and FM correlations compete, with the FM fluctuations gaining more weight upon approaching the charge-orbital order transition at T_{CO}. The coexistence of diffuse FM and CE-type correlations with different $\boldsymbol{Q}$ shapes indicates that microscopic phase separation occurs even in this pure half-doped material.

Inelastic fluctuations reminiscent of the CE-type order can be followed up to T_{CO}, but only the dispersion along the zigzag chains remains steep emphasizing once more the dominant role of the FM interaction along the zigzag chains. With the transition into the charge-orbital disordered phase above T_{CO}, the CE-type elastic and the inelastic correlations become fully suppressed. This behavior is fundamentally different from that of the magnetic stripelike fluctuations in the layered cuprates or nickelates, where inelastic magnetic correlations reminiscent of a static stripe phase can be observed far above the charge ordering or even in samples that actually do not exhibit static stripe ordering at all.[59–66] In $La_{1/2}Sr_{3/2}MnO_4$, the COO transition is of first order and apparently suppresses all traces of the complex low-temperature CE-type magnetic ground state. Instead of the CE-type magnetic fluctuations, strong isotropic in-plane FM correlations govern the charge-orbital disordered phase above T_{CO}. The sizable elastic diffuse scattering is directly related to the large magnetic susceptibility. In addition, there are well-defined inelastic fluctuations. It is remarkable that the dispersion of these FM correlations in the disordered phase of $La_{1/2}Sr_{3/2}MnO_4$ so closely resembles the magnon dispersion of the FM metallic perovskite phases. All our observations together underline the competition between FM and AFM CE-type magnetic correlations in $La_{1/2}Sr_{3/2}MnO_4$. These FM and AFM states are less different in character than one might naively think. The extra e_g electron per two Mn sites in $La_{1/2}Sr_{3/2}MnO_4$ constitutes the isotropic FM interaction in the charge-orbital disordered phase above T_{CO}; the same electron apparently also provides the dominant oriented FM interaction when it localizes in the orbital ordered phase.

The COO transition at T_{CO} is clearly associated with the crossover between FM and AFM CE-type correlations. However, it is difficult to decide whether these different magnetic fluctuations are just the consequence or the cause of the charge and orbital order transition. The fact that CE-type correlations are found immediately below T_{CO} may be taken as evidence for a magnetic mechanism of the COO transition. However, close to T_{CO}, the CE-type fluctuations are very weak (much weaker than at low temperature) and sizable, even stronger FM correlations remain closely below T_{CO}. This suggests that the transition into the charge and orbital ordered state is further driven by some nonmagnetic mechanism, as e.g., by Jahn–Teller distortions.

ACKNOWLEDGMENTS

This work was supported by the Deutsche Forschungsgemeinschaft through the Sonderforschungsbereich 608. We thank P. Reutler and D. Khomskii for numerous stimulating discussions as well as P. Baroni for technical support.

*Spektrometer PANDA, Institut für Festkörperphysik, TU Dresden.
†braden@ph2.uni-koeln.de

[1] A. J. Millis, P. B. Littlewood, and B. I. Shraiman, Phys. Rev. Lett. **74**, 5144 (1995).
[2] M. Uehara, S. Mori, C. H. Chen, and S.-W. Cheong, Nature (London) **399**, 560 (1999).
[3] A. Moreo, S. Yunoki, and E. Dagotto, Science **283**, 2034 (1999).
[4] F. M. Woodward, J. W. Lynn, M. B. Stone, R. Mahendiran, P. Schiffer, J. F. Mitchell, D. N. Argyriou, and L. C. Chapon, Phys. Rev. B **70**, 174433 (2004).
[5] G. C. Milward, M. J. Calderón, and P. B. Littlewood, Nature (London) **433**, 607 (2005).
[6] C. Şen, G. Alvarez, and E. Dagotto, Phys. Rev. Lett. **98**, 127202 (2007).
[7] Y. Tokura and N. Nagaosa, Science **288**, 462 (2000).
[8] S. Murakami and N. Nagaosa, Phys. Rev. Lett. **90**, 197201 (2003).
[9] B. J. Sternlieb, J. P. Hill, U. C. Wildgruber, G. M. Luke, B. Nachumi, Y. Moritomo, and Y. Tokura, Phys. Rev. Lett. **76**, 2169 (1996).
[10] D. N. Argyriou, H. N. Bordallo, B. J. Campbell, A. K. Cheetham, D. E. Cox, J. S. Gardner, K. Hanif, A. dos Santos, and G. F. Strouse, Phys. Rev. B **61**, 15269 (2000).
[11] E. O. Wollan and W. C. Koehler, Phys. Rev. **100**, 545 (1955).
[12] J. B. Goodenough, Phys. Rev. **100**, 564 (1955).
[13] P. G. Radaelli, D. E. Cox, M. Marezio, and S.-W. Cheong, Phys. Rev. B **55**, 3015 (1997).
[14] Y. Murakami, H. Kawada, H. Kawata, M. Tanaka, T. Arima, Y. Moritomo, and Y. Tokura, Phys. Rev. Lett. **80**, 1932 (1998).
[15] A. Daoud-Aladine, J. Rodríguez-Carvajal, L. Pinsard-Gaudart, M. T. Fernández-Díaz, and A. Revcolevschi, Phys. Rev. Lett. **89**, 097205 (2002).
[16] D. Efremov, J. van den Brink, and D. Khomskii, Nat. Mater. **3**, 853 (2004).
[17] S. Grenier, J. P. Hill, D. Gibbs, K. J. Thomas, M. v. Zimmermann, C. S. Nelson, V. Kiryukhin, Y. Tokura, Y. Tomioka, D. Casa, T. Gog, and C. Venkataraman, Phys. Rev. B **69**, 134419 (2004).
[18] R. J. Goff and J. P. Attfield, Phys. Rev. B **70**, 140404(R) (2004).
[19] E. E. Rodriguez, T. Proffen, A. Llobet, J. J. Rhyne, and J. F. Mitchell, Phys. Rev. B **71**, 104430 (2005).
[20] D. Senff, F. Krüger, S. Scheidl, M. Benomar, Y. Sidis, F. Demmel, and M. Braden, Phys. Rev. Lett. **96**, 257201 (2006).
[21] A. Trokiner, A. Yakubovskii, S. Verkhovskii, A. Gerashenko, and D. Khomskii, Phys. Rev. B **74**, 092403 (2006).
[22] Z. Jirak, S. Krupicka, Z. Simsa, M. Dlouha, and S. Vraatislav, J. Magn. Magn. Mater. **53**, 153 (1985).
[23] F. Damay, Z. Jirak, M. Hervieu, C. Martin, A. Maignan, B. Raveau, G. André, and F. Bourrée, J. Magn. Magn. Mater. **190**, 221 (1998).
[24] Z. Jirak, F. Damay, M. Hervieu, C. Martin, B. Raveau, G. André, and F. Bourée, Phys. Rev. B **61**, 1181 (2000).
[25] O. Schumann, D. Senff, M. Benomar, and M. Braden (unpublished).
[26] S. Yunoki, T. Hotta, and E. Dagotto, Phys. Rev. Lett. **84**, 3714 (2000).
[27] Z. Popović and S. Satpathy, Phys. Rev. Lett. **88**, 197201 (2002).
[28] S. Dong, S. Dai, X. Y. Yao, K. F. Wang, C. Zhu, and J.-M. Liu, Phys. Rev. B **73**, 104404 (2006).
[29] I. V. Solovyev and K. Terakura, Phys. Rev. Lett. **83**, 2825 (1999).
[30] J. van den Brink, G. Khaliullin, and D. Khomskii, Phys. Rev. Lett. **83**, 5118 (1999).
[31] I. V. Solovyev, Phys. Rev. Lett. **91**, 177201 (2003).
[32] I. V. Solovyev, Phys. Rev. B **63**, 174406 (2001).
[33] S. Larochelle, A. Mehta, N. Kaneko, P. K. Mang, A. F. Panchula, L. Zhou, J. Arthur, and M. Greven, Phys. Rev. Lett. **87**, 095502 (2001).
[34] P. Mahadevan, K. Terakura, and D. D. Sarma, Phys. Rev. Lett. **87**, 066404 (2001).
[35] S. B. Wilkins, P. D. Spencer, P. D. Hatton, S. P. Collins, M. D. Roper, D. Prabhakaran, and A. T. Boothroyd, Phys. Rev. Lett. **91**, 167205 (2003).
[36] S. S. Dhesi, A. Mirone, C. De Nadai, P. Ohresser, N. B. Brookes, P. Reutler, A. Revcolevschi, A. Tagliaferri, O. Toulemonde, and G. van der Laan, Phys. Rev. Lett. **92**, 056403 (2004).
[37] M. Tokunaga, N. Miura, Y. Moritomo, and Y. Tokura, Phys. Rev. B **59**, 11151 (1999).
[38] Y. Moritomo, Y. Tomioka, A. Asamitsu, Y. Tokura, and Y. Matsui, Phys. Rev. B **51**, 3297 (1995).
[39] S. Larochelle, A. Mehta, L. Lu, P. K. Mang, O. P. Vajk, N. Kaneko, J. W. Lynn, L. Zhou, and M. Greven, Phys. Rev. B **71**, 024435 (2005).
[40] D. Senff, P. Reutler, M. Braden, O. Friedt, D. Bruns, A. Cousson, F. Bouree, M. Merz, B. Büchner, and A. Revcolevschi, Phys. Rev. B **71**, 024425 (2005).
[41] P. Reutler, O. Friedt, B. Büchner, M. Braden, and A. Revcolevschi, J. Cryst. Growth **249**, 222 (2003).
[42] K. Marumoto, K. Soda, S. Kuroda, and Y. Moritomo, J. Phys. Soc. Jpn. **72**, 582 (2003).
[43] R. M. Moon, T. Riste, and C. Koehler, Phys. Rev. **181**, 920 (1969).
[44] P. Reutler, Y. Sidis, and M. Braden (unpublished).
[45] *Magnetic Properties of Layered Transition Metal Compounds*, edited by L. J. de Jongh (Kluwer, Dordrecht,1989).
[46] N. E. Bonesteel, Phys. Rev. B **47**, 11302 (1993).
[47] A. Zheludev, *ResLib 3.3* (Oak Ridge National Laboratory, Oak Ridge, 2006).
[48] T. G. Perring, G. Aeppli, S. M. Hayden, S. A. Carter, J. P. Remeika, and S.-W. Cheong, Phys. Rev. Lett. **77**, 711 (1996).
[49] V. V. Krishnamurthy, J. L. Robertson, R. S. Fishmann, M. D. Lumsden, and J. F. Mitchell, Phys. Rev. B **73**, 060404(R) (2006).
[50] H. Yoshizawa, H. Kawano, J. A. Fernandez-Baca, H. Kuwahara, and Y. Tokura, Phys. Rev. B **58**, R571 (1998).
[51] F. Ye, P. Dai, J. A. Fernandez-Baca, H. Sha, J. W. Lynn, H. Kawano-Furukawa, Y. Tomioka, Y. Tokura, and J. Zhang, Phys. Rev. Lett. **96**, 047204 (2006).
[52] R. Mathieu, M. Uchida, Y. Kaneko, J. P. He, X. Z. Yu, R. Kumai, T. Arima, Y. Tomioka, A. Asamitsu, Y. Matsui, and Y. Tokura, Phys. Rev. B **74**, 020404(R) (2006).
[53] J.-C. Bouloux, J.-L. Soubeyroux, A. Daouda, and G. Le Flem, Mater. Res. Bull. **16**, 855 (1981).
[54] N. Kumar and C. N. R. Rao, J. Solid State Chem. **129**, 363 (1997).
[55] W. Bao, J. D. Axe, C. H. Chen, and S.-W. Cheong, Phys. Rev. Lett. **78**, 543 (1997).
[56] F. Millange, S. de Brion, and G. Chouteau, Phys. Rev. B **62**, 5619 (2000).
[57] Y. Tomioka and Y. Tokura, Phys. Rev. B **66**, 104416 (2002).

[58] F. Ye, J. A. Fernandez-Baca, P. Dai, J. W. Lynn, H. Kawano-Furukawa, H. Yoshizawa, Y. Tomioka, and Y. Tokura, Phys. Rev. B **72**, 212404 (2005).
[59] C. H. Chen, S.-W. Cheong, and A. S. Cooper, Phys. Rev. Lett. **71**, 2461 (1993).
[60] V. Sachan, D. J. Buttrey, J. M. Tranquada, J. E. Lorenzo, and G. Shirane, Phys. Rev. B **51**, 12742 (1995).
[61] J. M. Tranquada, D. J. Buttrey, and V. Sachan, Phys. Rev. B **54**, 12318 (1996).
[62] P. Bourges, Y. Sidis, M. Braden, K. Nakajima, and J. M. Tranquada, Phys. Rev. Lett. **90**, 147202 (2003).
[63] S.-W. Cheong, G. Aeppli, T. E. Mason, H. Mook, S. M. Hayden, P. C. Canfield, Z. Fisk, K. N. Clausen, and J. L. Martinez, Phys. Rev. Lett. **67**, 1791 (1991).
[64] J. M. Tranquada, B. J. Sternlieb, J. D. Axe, Y. Nakamura, and S. Uchida, Nature (London) **375**, 561 (1995).
[65] K. Nakajima, K. Yamada, S. Hosoya, Y. Endoh, M. Greven, and R. J. Birgenau, Z. Phys. B: Condens. Matter **96**, 479 (1995).
[66] J. M. Tranquada, P. Wochner, and D. J. Buttrey, Phys. Rev. Lett. **79**, 2133 (1997).
[67] W. Reichardt and M. Braden, Physica B (Amsterdam) **263-264**, 416 (1999).
[68] L. Brey, Phys. Rev. B **71**, 174426 (2005).
[69] M. Daghofer, A. M. Oles, D. R. Neuber, and W. von der Linden, Phys. Rev. B **73**, 104451 (2006).